Available online at www.sciencedirect.com
SCIENCE DIRECT®
Pergamon
Acta Materialia 51 (2003) 4197–4208
Acta MATERIALIA
www.actamat-journals.com

Nanostructured Al–Fe alloys produced by e-beam deposition: static and dynamic tensile properties

T. Mukai [a,*1], S. Suresh [a], K. Kita [b], H. Sasaki [b], N. Kobayashi [b], K. Higashi [c], A. Inoue [d]

[a] *Department of Materials Science and Engineering, Massachusetts Institute of Technology, Cambridge, MA 02139-4307, USA*
[b] *Sendai Institute of Materials Science and Technology, YKK Corporation, Kurokawa 981-3341, Japan*
[c] *Department of Metallurgy and Materials Science, Osaka Prefecture University, Osaka 599-8531, Japan*
[d] *Institute for Materials Research, Tohoku University, Sendai 980-8577, Japan*

Received 4 September 2002; received in revised form 20 March 2003; accepted 10 April 2003

Abstract

Three different aluminum–iron alloys were produced by electron-beam deposition with the iron content in the range 1.15–1.71 at.%. These alloys did not contain any identifiable iron-bearing particles, and exhibited full density with high-angle grain boundaries in the micrometer range, and a sub-grain size typically smaller than 100 nm. The tensile deformation characteristics of the alloys were examined at a dynamic strain rate of 1.1×10^3 s^{-1} and a quasi-static strain rate of 1×10^{-3} s^{-1} at room temperature. The alloy containing 1.7% Fe exhibited an abnormally high tensile strength of about 950 MPa with a ductility of up to 6%. Detailed atomic resolution imaging of the structure of the alloys has been performed along with an examination of their fracture surface features. The fracture surfaces of the alloys showed ductile dimples which typically spanned five to 10 times the sub-grain diameter. It is postulated that the nano-scale sub-grains of the alloy impart high strength, while the structure associated with high-angle boundaries provides reasonable ductility. Possible mechanisms responsible for the high strength in the present Al–Fe alloys are explored. The present results are also examined in conjunction with a comprehensive survey of available results on the strain-rate sensitivity of tensile yield strength and ductility in microcrystalline, sub-microcrystalline and nanocrystalline metals and alloys, and on the solid-solution strengthening of aluminum alloys.

Keywords: Nanocrystalline alloy; Dynamic tensile loading; Solution strengthening; Ductility; e-Beam deposition

1. Introduction

Nanocrystalline metals and alloys, with average grain size values typically below 100 nm, are the focus of increasing research activity owing to their promise for superior performance in a variety of mechanical, environmental, tribological and mag-

* Corresponding author. Tel.: +81-3-5452-5486; fax: +81-3-5452-5486.
E-mail address: toshiji@pp.iij4u.ur.jp (T. Mukai).
[1] Present address: Research Center for Advanced Science and Technology, The University of Tokyo, 4-6-1 Komaba Meguro-ku, Tokyo 153-8904, Japan.

1359-6454/03/$30.00 © 2003 Acta Materialia Inc. Published by Elsevier Ltd. All rights reserved.
doi:10.1016/S1359-6454(03)00237-4

netic applications in comparison to conventional microcrystalline metals and alloys. Available methods for the processing of nanocrystalline metal alloys can be classified into different broad categories: (a) powder metallurgy methods which include inert gas condensation and consolidation of nanopowders [1–3] and mechanical alloying [4–8], (b) crystallization of an initially amorphous material [9,10], (c) mechanical metallurgy methods involving severe plastic deformation of initially microcrystalline alloys [11,12], such as by equal-channel-angular pressing (ECAP), and (d) deposition methods such as electrodeposition [13–15], or physical vapor deposition [16]. Powder metallurgy methods typically suffer from the limitation that the consolidated nanostructured alloy is not of full density, and that processing-induced porosity can curtail ductility and fracture resistance. Crystallization of an initially amorphous structure does not provide the flexibility to produce nanocrystalline alloys of broad composition ranges and properties. Severe plastic deformation often results in an as-processed microstructure with a high initial dislocation density, large residual stress, and, in many cases, a non-uniform grain and defect distribution. Deposition methods offer the possibility to produce clean, fully dense nanocrystalline metallic materials with a narrow range of grain sizes and large in-plane dimensions, although the thickness of the specimens so produced is no more than a few millimeters; in addition, methods such as electrodeposition can introduce contamination from hydrogen, sulfur or other impurities.

Despite the availability of these various processing methods, the basic mechanical deformation characteristics of nanocrystalline metals are not fully understood at this time. This situation is in part due to the paucity of systematic and detailed deformation experiments spanning a wide range of loading modes (tension, compression, multi-axial, cyclic, etc.), strain rates (from quasi-static to dynamic) and temperature. A topic of particular interest for the development of constitutive models for the mechanical response of nanocrystalline metal alloys involves the dependence of overall deformation on strain-rate sensitivity. Such studies are of scientific and practical interest on several counts. (1) Experimental and mechanistic studies of strain-rate sensitivity provide the most fundamental information on time-dependent and time-independent deformation. (2) Many structural applications for which the nanocrystalline alloys are potential candidates inevitably require knowledge of their resistance to impact and foreign object damage. (3) Many of the potentially beneficial characteristics of nanocrystalline materials, such as high yield strength, hardness and resistance to tribological contact, have not been explored in sufficient detail over the range of strain rates of practical interest. (4) Focused studies of rate sensitivity and work hardening behavior at different strain rates offer unique probes into the micromechanisms controlling defect generation and damage evolution.

To date, only a limited number of investigators have examined the strain-rate sensitivity of nanocrystalline materials. Gray et al. [17] performed dynamic compression of sub-micron-grained pure Cu and Ni using ECAP, and demonstrated that the materials exhibited pronounced strain-rate sensitivity and no strain hardening. In contrast to this result for face-centered cubic metals, Jia et al. [5] showed that nanocrystalline body-centered cubic Fe produced by mechanical milling (MM), with an average grain size of 80 nm, is only weakly strain-rate sensitive in compression, and that it is characterized by high strength, limited elongation-to-failure where deformation is localized in shear bands, and no strain hardening. Note that mechanical milling also produces a microstructure with significant initial deformation and high dislocation density. Lu et al. [15] demonstrated the enhancement of ductility and strength with increasing strain rate in electrodeposited nanocrystalline pure copper with an average grain size of approximately 20 nm. Subsequent studies of compression deformation by Jia et al. [18] revealed that nanocrystalline pure copper exhibits significant strain hardening and strain rate dependence of ductility, although the yield stress is almost independent of strain rate. Superplastic forming of ECAP-processed nanocrystalline Ni and Ni–Al alloys under high strain rates at low temperatures has also been demonstrated [19]. To our knowledge, however, no studies have thus far been reported in the open literature on the strain-rate sensitivity of pure tensile deformation

in nanocrystalline metal alloys. Furthermore, the mechanisms underlying any effects of loading rate on deformation have not been explored in sufficient detail.

In the past three decades, Al–Fe binary and Al–Fe-based multi-component alloys have been extensively investigated for aerospace applications at elevated temperature [20–24]. The alloys, such as Al–Fe–Ce [23] and Al–Fe–V [24], maintain high strength up to about 573 K owing to the presence of thermally stable second phases with submicrometer size. However, large amounts of second phases often provide stress concentrations for damage evolution, and serve as nucleation sites for cracks, especially under dynamic loading [10]. A previous study aimed at producing Al–Fe binary alloys by using electron-beam deposition revealed that the microstructure was refined with increasing concentration of iron, and a very fine-grained structure without second-phase particles was formed with a content of 1–3 at.% iron [16]. In this prior work, tensile deformation at high strain rates was not investigated. While the study focused on microstructural evolution and strengthening due to increase in the concentration of iron, the effects of Fe content on ductility in both quasi-static and dynamic tension were also not investigated. In this paper, we present the stress–strain characteristics of nanocrystalline Al–Fe solid-solution alloys subjected to quasi-static and high-strain-rate tensile deformation and demonstrate the enhancement of strength and ductility in the metastable single-phase alloy compared to microcrystalline aluminum alloys. The dynamic tensile experiments were conducted at a strain rate of approximately $10^3\ s^{-1}$. For comparison purposes, quasi-static tensile experiments were also conducted on each of the alloys. X-ray diffraction (XRD) and transmission electron microscopy (TEM) were performed on the as-deposited materials, and the tensile fracture surfaces were studied in a scanning electron microscope in an attempt to elucidate the mechanisms of deformation.

2. Materials and experimental methods

The electron-beam evaporation process has the highest rate of deposition compared with other physical vapor deposition (PVD) techniques. A continuous supply of rod-shaped evaporation sources was used to produce bulk plate specimens with dimensions of 100 mm × 100 mm × 0.6 mm. Full details on the experimental procedures can be found elsewhere [16].

Supersaturated Al–Fe solid-solution alloys were prepared by PVD using two electron-beam evaporation sources. The composition of each deposit was controlled by changing the proportions of Al and Fe deposition rates by adjusting the energy of the electron beam in relation to each evaporation source. In the present study, the alloys were approximately 0.6 mm in thickness after deposition runs of 12.6 ks. Prior research has shown that high Fe content (typically more than 5 at.%) in Al induces the formation of an amorphous structure, while Fe content of less than 3 at.% produces a controlled polycrystalline structure [16]. In the current study, the measured concentrations of iron after deposition were found to be 1.15, 1.53 and 1.71 at.% in the three alloys. The structures of the as-deposited alloys were examined by XRD and TEM.

Tensile mechanical properties were examined at room temperature. The tensile specimen had a gauge length of 9 mm, width of 3 mm and thickness of 0.6 mm. In order to examine the strain-rate sensitivity, tensile tests were carried out at a dynamic strain rate of $1.1 \times 10^3\ s^{-1}$ and a quasi-static strain rate of $1 \times 10^{-3}\ s^{-1}$. The dynamic tensile tests were conducted using a tensile Hopkinson bar apparatus [25], which was made of tool steel bars with a diameter of 16 mm and length of 2 m. Dynamic loading was introduced by targeting a brass projectile at a flange connected to the tensile specimen.

3. Experimental results

In order to characterize the morphology and grain size of the alloys, the microstructure was inspected by an optical microscope and TEM. All three alloys were found to consist of grains, approximately 2 μm in diameter, surrounded by high-angle grain boundaries. Microstructural observation with TEM and selected area diffraction

pattern (SAD) revealed the presence of sub-grains in all three alloys. The sub-grain structures are shown in Fig. 1(a), (b) and (c) for the Al–1.15 at.% Fe, Al–1.53 at.% Fe, and Al–1.71 at.% Fe alloys, respectively. These three alloys will hereafter be denoted as Al–1.2Fe, Al–1.5Fe and Al–1.7Fe, respectively. The average sub-grain sizes of the present alloys were similar in the nano-scale range, and slightly refined from 95 to 85 nm with increasing Fe content from 1.15 to 1.71 at.%. The XRD pattern for the Al–1.7Fe alloy is shown in Fig. 2, where only the α-Al crystalline peaks are seen; no peaks of any second phase are observed. Since the same trend was also exhibited by all the Al–Fe alloys with Fe content less than 3.0 at.%, these XRD patterns along with TEM observations (presented in later sections) reveal that the as-deposited alloys used in this study were composed of a single phase.

Nominal stress–strain relations of Al–1.2Fe, Al–1.5Fe and Al–1.7Fe alloys at a quasi-static strain rate of 1×10^{-3} s^{-1} and a dynamic strain rate of 1.1×10^{3} s^{-1} are shown in Fig. 3. Note that the flow stress values of the present nanocrystalline Al–Fe alloys are higher than those of conventional microcrystalline Al alloys, and that the flow stress increases with increasing content of Fe at both strain rates. The flow stress at the dynamic strain rate exhibits a higher value than that at the quasi-static strain rate for the Al–Fe alloys, although the initial yield stress is essentially independent of strain rate. The as-deposited nanocrystalline Al–1.7Fe alloy shows an abnormally high tensile strength of ~950 MPa and ductility of ~6% in tension at the dynamic strain rate. Note that the tensile strain to failure at the dynamic strain rate is essentially the same as that at the quasi-static strain rate for the same alloy. The three alloys examined in this work exhibit only slightly positive strain-rate sensitivity of initial yield strength and ductility. A higher hardening rate is observed in all these alloys at the dynamic strain rate.

An examination of the fractured specimen of the Al–1.5Fe alloy after the dynamic tensile test revealed that the final fracture event occurred at a macroscopic shear plane inclined more than 45° with respect to the tensile axis, indicating the formation of localized shear bands (Fig. 4). The speci-

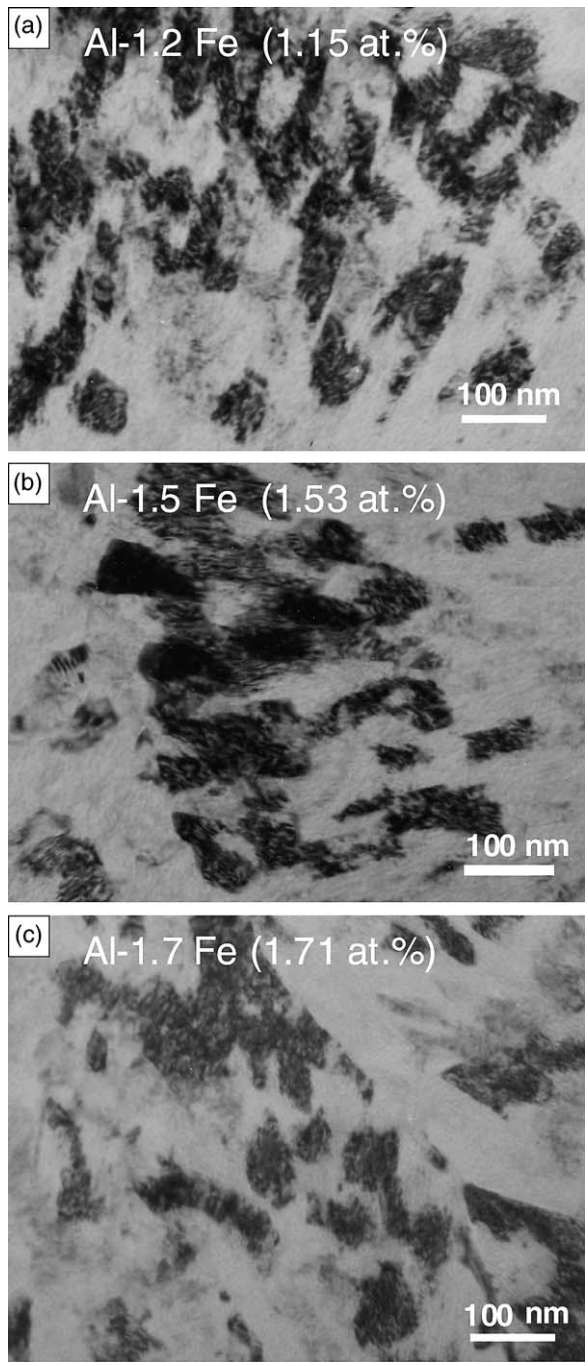

Fig. 1. TEM microstructures of (a) Al–1.2Fe, (b) Al–1.5Fe and (c) Al–1.7Fe alloys. The sub-grains are typically smaller than 100 nm in size.

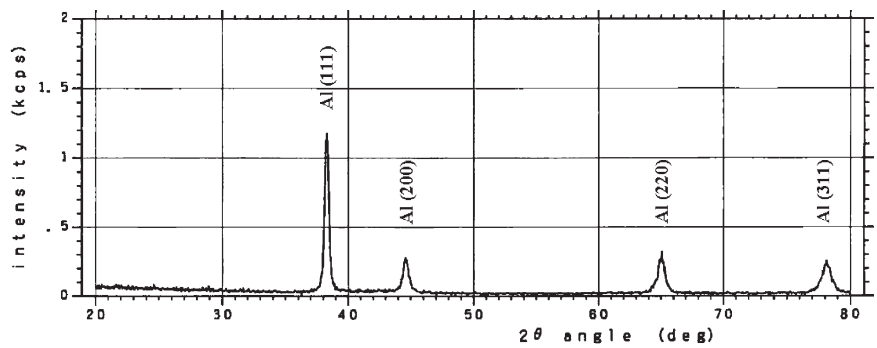

Fig. 2. X-ray diffraction pattern of Al–1.7Fe alloy. The peaks indicate only α-Al solid-solution alloy and no identifiable second phase.

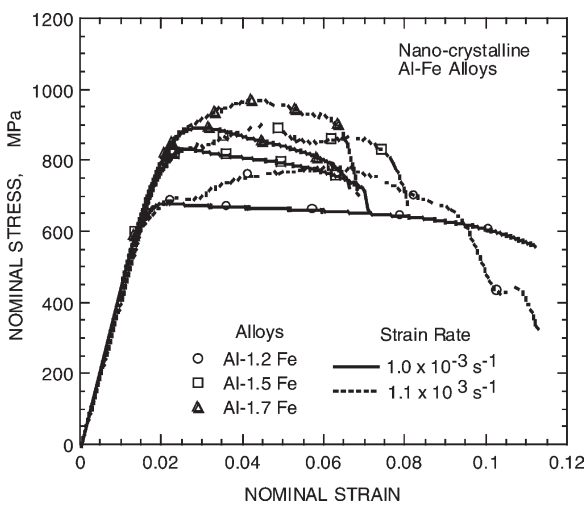

Fig. 3. Experimentally determined nominal stress–strain curves for the Al–1.2Fe, Al–1.5Fe and Al–1.7Fe alloys at a quasi-static strain rate of 1×10^{-3} s^{-1} and a dynamic strain rate of 1.1×10^{3} s^{-1}.

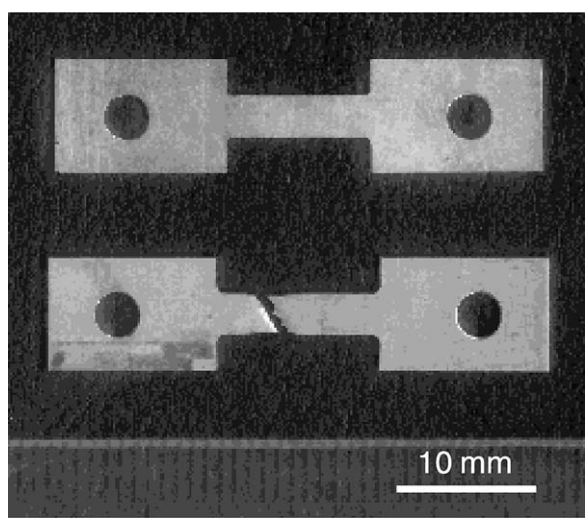

Fig. 4. Appearance of the fractured tensile specimen of Al–1.5Fe alloy. The upper figure is the undeformed specimen and the lower figure shows the specimen after the tensile test at the dynamic strain rate of 1.1×10^{3} s^{-1}.

men also exhibited a macroscopic necking near the fracture surface, especially in the plate thickness direction. Similar features could also be seen for all the specimens examined at both quasi-static and dynamic strain rates.

The fracture surfaces of Al–1.7Fe alloy from the quasi-static and dynamic tests are shown in Fig. 5(a) and (b), respectively. These images clearly indicate that the local failure process is ductile in the nanocrystalline Al–Fe alloys fractured both quasi-statically and dynamically, with the mechanism of failure arising from the nucleation, growth and coalescence of voids. The dimple sizes at two strain rates are also found to be five to 10 times the sub-grain size of the present alloys.

The addition of Fe, beyond a certain critical concentration, to an aluminum matrix is known to lead to the formation of Fe-bearing precipitates and inclusions. To illustrate this effect, Fig. 6 shows a high-resolution transmission electron micrograph of a reference alloy with a composition, Al–3 at.% Fe, which was produced by e-beam evaporation using the same procedure, substrate temperature and deposition rates as the three alloys of lower Fe content investigated in this work. The parallelo-

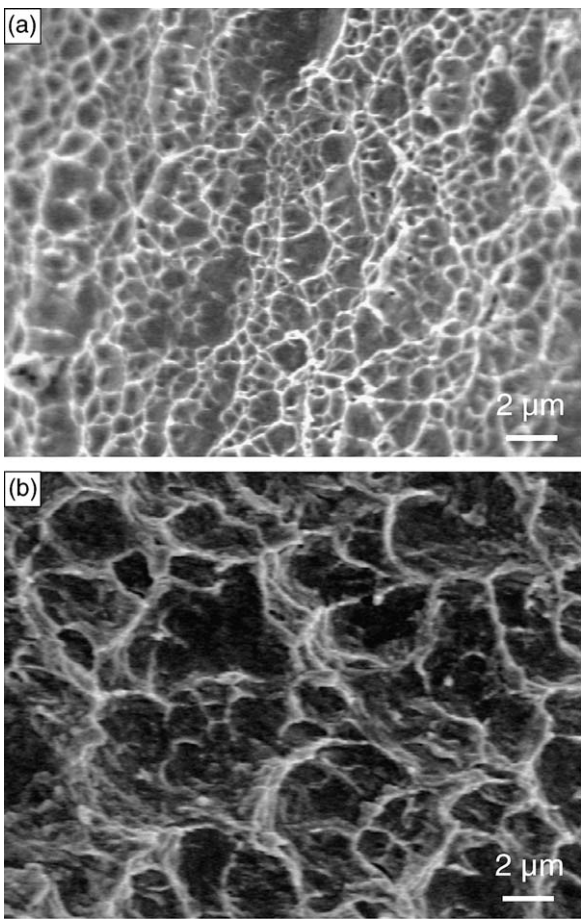

Fig. 5. Fracture surface of the Al–1.7Fe alloy deformed (a) at a quasi-static strain rate of 1×10^{-3} s^{-1} and (b) at a dynamic strain rate of 1.1×10^{3} s^{-1}.

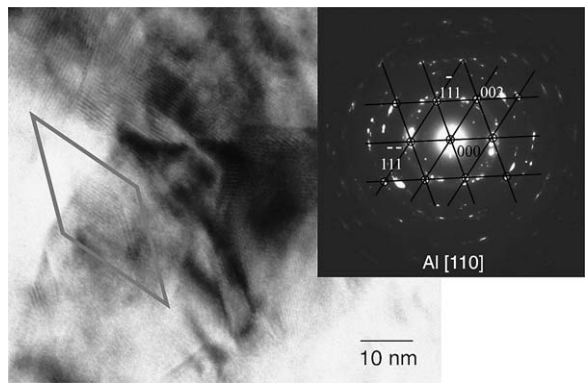

Fig. 6. Example of the formation of an iron-bearing particle in the matrix of a reference alloy with a composition of Al–3 at.% Fe. The particle is indicated by the dashed parallelogram. Also shown is the SAD pattern of this reference alloy where evidence for the presence of the particles can be seen.

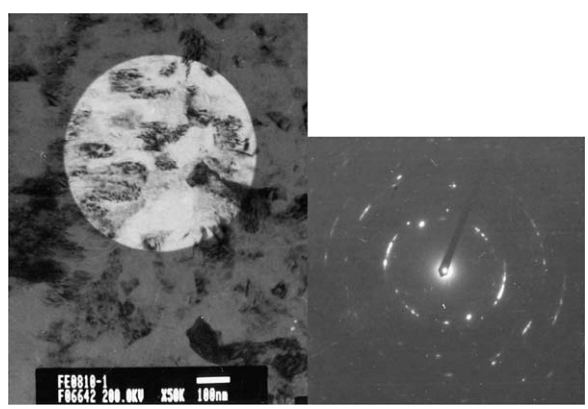

Fig. 7. Selected area diffraction pattern of Al–1.5Fe alloy. Compare this SAD pattern with that shown in the reference Al–3Fe alloy in Fig. 6, and note the absence of any patterns associated with a second phase.

gram sketched in this figure encircles an Fe-containing particle which was formed in this reference alloy with 3 at.% Fe. Also shown in the inset to this figure is the SAD pattern of a region of this alloy. The pattern shows diffraction spots which reveal the presence of the particle.

By contrast, Fig. 7 shows a region of the present Al–1.5Fe solid-solution alloy. Also shown in the figure are the SAD patterns of the alloy. When this figure is compared to Fig. 6, it is readily apparent that the SAD patterns associated with the formation of second-phase particles, seen in Fig. 6, are completely absent in Fig. 7. The pattern shows only α-Al and no evidence of second-phase particles. Similar SAD patterns were observed for the other regions in the Al–1.5Fe alloy and for the other two alloys studied in this work.

The initial microstructure of Al–1.5Fe is shown in Fig. 8 at a higher magnification, where regions of lattice distortion are seen in the interior of the grain. An atomic resolution image of Al–1.5Fe alloy is also shown in Fig. 9, where the regions enveloped by the white ovals denote lattice sites where the aluminum solid-solution matrix is disrupted by the possible presence of defects or clusters of Fe atoms. Note the absence of cross fringes in the regions encompassed by these ovals. The

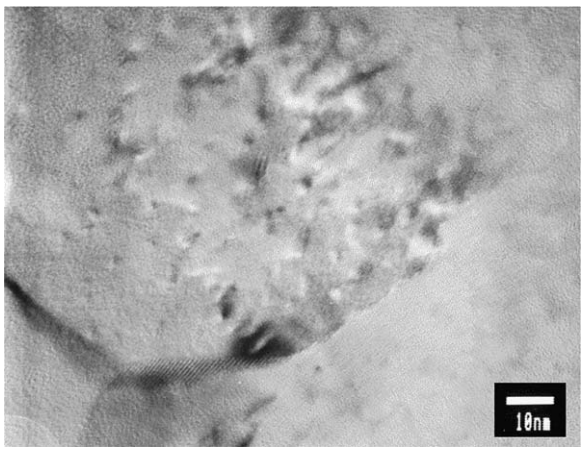

Fig. 8. Initial grain structure of Al–1.5Fe alloy at a high magnification.

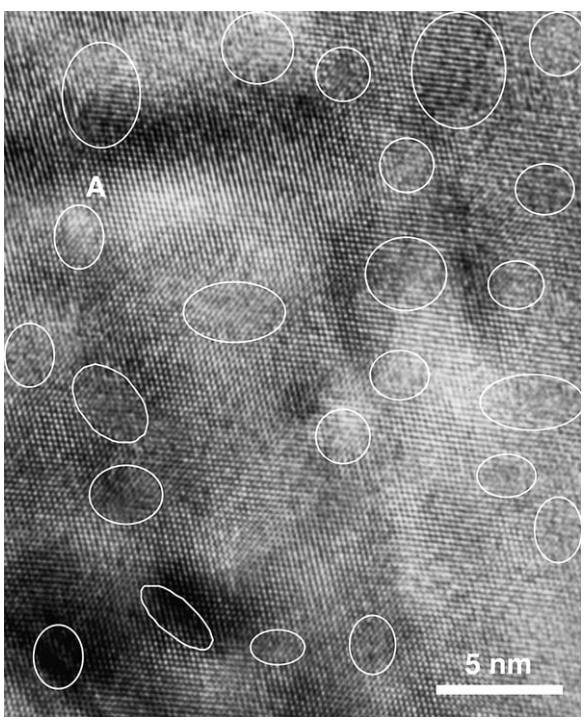

Fig. 9. Lattice image of the Al–1.5Fe alloy. The white ovals indicate zones that comprise the aluminum lattice disrupted by the possible presence of defects, clusters of the alloy atoms or nano-scale precipitates.

size of these zones and their mean spacing are measured from this image to be approximately 1 and 7 nm, respectively. A high-magnification image of the region marked A in Fig. 9 is shown in Fig. 10, where atomic planes are marked by specific numbers. It is seen that these white lines marked on the figure are slightly bent as one traverses from the top to the bottom of the figure. A defect which lies in a direction normal to the plane of the figure could have formed near the center of Fig. 10. The existence of defects can thus strongly affect the lattice; in Fig. 10, the bending of the lattice is estimated to be about 1°. The bent lattice can cause the formation of a fringe-like pattern in the interior of grains, as can be seen in Fig. 1. The formation of low-angle boundaries (e.g. Fig. 1) is also expected from the presence of a large population of such defects in the present alloys. Although the nature and origin of the defects (that is, whether they are clusters of solute atoms or nano-scale precipitates) is not fully understood at the present time, the microstructure of the present alloy is noted to be distinctly different from that of some rapidly solidified Al–Fe [20,22] or Al–Fe–X [21–24] alloys studied previously.

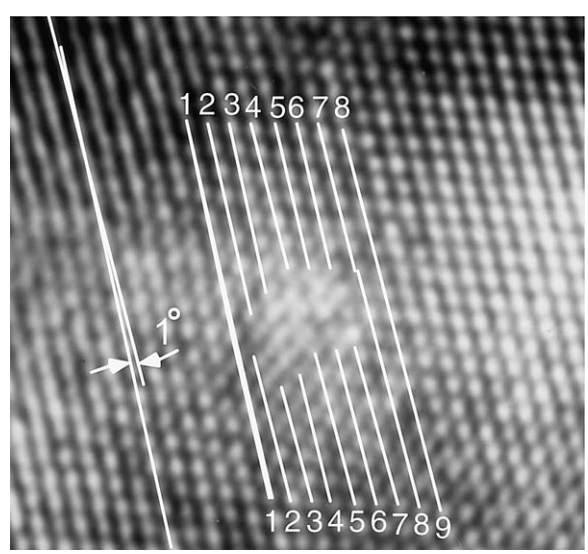

Fig. 10. Higher magnification image of the zone marked A in Fig. 9. Evidence of lattice mismatch is shown. Lattice bending in the vicinity of lattice mismatch is also seen.

4. Discussion

The variation of initial yield stress, normalized by the value at the slowest strain rate, is plotted in Fig. 11 as a function of strain rate for the present Al–Fe alloy. Also shown in this plot are available results from the literature for microcrystalline (MC) metals and alloys [15,26–28], sub-microcrystalline (SMC) metals and alloys, with grain size typically in the 100 nm–1 μm range [17,29,30], and nanocrystalline (NC) metals [6,15,31]. The normalized initial yield stress of the present NC Al–Fe alloy is essentially independent of strain rate just as those of some SMC alloys, while those for the MC alloys exhibit certain strain-rate sensitivity. The SMC alloys, processed by ECAP or mechanical alloying, induce a large residual stress and a high dislocation density in the as-processed microstructure. The dislocations generated during deformation of these materials are easily obstructed by dislocation networks, which is possibly a consequence of the weak strain-rate sensitivity of flow stress. The yield stress of the present Al–Fe alloys exhibits a similar strain-rate sensitivity. Thus, it is conceivable that the solute Fe atoms possibly form a barrier against dislocation motion. This notion is further reinforced by the result that nanocrystalline pure metals, such as Mg [6], Ni [31] and Cu [15], which do not have such impurity clusters, also exhibit stronger strain-rate sensitivity of initial yield stress which is absent in the nanocrystalline Al–Fe alloys.

The variation of tensile ductility, normalized by the strain-to-failure at the slowest strain rate, is plotted in Fig. 12 as a function of strain rate for the present Al–Fe alloy. Also plotted in this figure for comparison are the tensile ductility results for MC metals and alloys [15,27,29], SMC metals and alloys [29,30], and NC pure metals [15,31]. Contrary to the result of MC-Cu [15], MC-Al alloys [27,29] and SMC-Al alloys [29,30] exhibit pronounced strain-rate sensitivity, which is highlighted by the shaded region in Fig. 12. The ductility enhancement of MC- and SMC-Al alloys has been ascribed to the extended uniform deformation arising from the movement of lattice dislocations with increasing strain rate [30]. On the other hand, NC-Cu [15] and Ni [31] exhibit higher strain-rate sensitivity of ductility. The result suggests that the deformation mechanism in NC pure metals is likely dominated by grain boundaries rather than

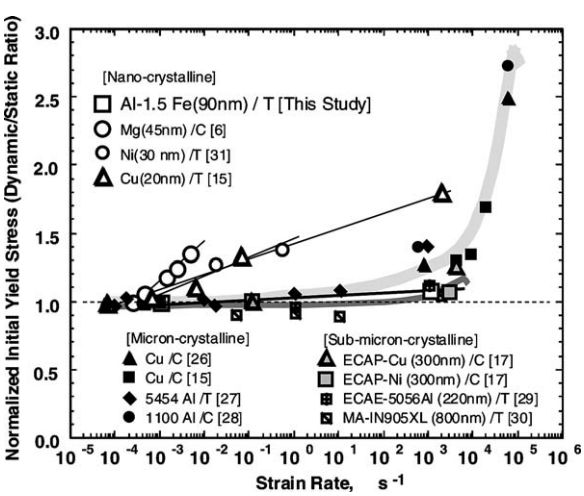

Fig. 11. Variation of normalized yield stress (each stress divided by that at the slowest strain rate) as a function of strain rate for the present Al–Fe alloy. Also included in the figure are data for micron-scale-crystalline metal and alloys [15,26–28], sub-microcrystalline metals and alloys [17,29,30] and nanocrystalline metals [6,15,31]. In the legend, C and T indicate the loading conditions of compression and tension, respectively.

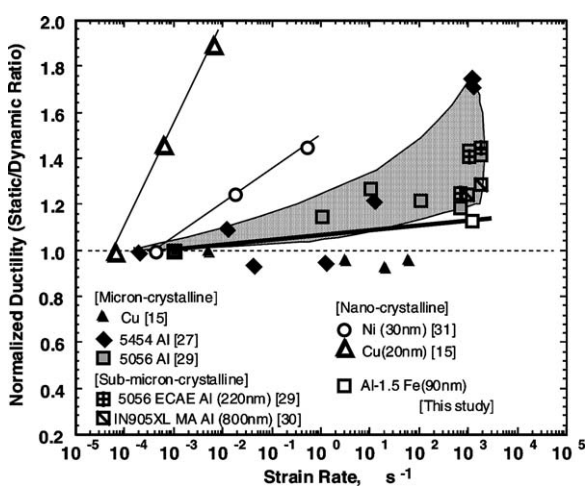

Fig. 12. Variation of normalized ductility (each elongation-to-failure divided by that at the slowest strain rate) as a function of strain rate for the present Al–Fe alloy. Including are the data for micron-scale-crystalline metal and alloys [15,27,29], sub-microcrystalline metals and alloys [29,30] and nanocrystalline metals [15,31].

by lattice dislocations [32]. The strain-rate sensitivity in the present NC Al–Fe alloy is also weakly positive, but limited, which suggests that the dominant deformation mechanism in NC solid-solution Al–Fe alloy may be very different from that of NC pure metals. It should also be noted that the grain size of NC-Cu [15] and NC-Ni [31] are smaller than that of the present Al–Fe alloys, and that the differences in the grain sizes among these alloys could also influence the observed differences in strain-rate sensitivity.

Table 1 provides a comparison of the strength and strain to failure values of the present Al–Fe alloys with nano-scale sub-grains with those of other Al–Fe alloys [22–24,33,34] and high-strength aluminum alloys [7–10,35–39]. For the present alloys, the presence of Fe solute atom is a key factor in the formation of the nanocrystalline structure and the high tensile strength. The microstructure of vapor-quenched aluminum alloys was extensively investigated by Bickerdike et al. [34,36] and the mechanical properties were examined by Partridge et al. [33,37]. They also studied the Al–Fe binary alloy. Their binary Al–Fe alloy was fabricated with a heated crucible and collector which was rotated about a vertical axis about 20 mm above the evaporators [34]. Owing to the short distance between the collector and evaporator, the as-deposited Al–Fe alloys consisted of Al-rich and Fe-rich two-phase layers, with a thickness of 43–197 nm and 0.3–2.9 nm, respectively. Before the examination of mechanical properties, the as-deposited alloys were hot-pressed and hot-rolled to eliminate the Fe-rich layer. The hot-worked alloys contained fine metastable Al_6Fe particles with a diameter of 50–200 nm [33]. Although the grain size of the matrix was not reported, the grain size was presumably larger than that of dispersoids. For the fabrication of the present alloys, the collector was rotated about a vertical axis with a distance of 150 mm to the evaporators. Thus, the deposited materials did not form any Al- and Fe-rich layered phases.

Supersaturated Al–Fe alloys have also been fabricated by the splat quenching route [22,38]. Nasu et al. [38] reported evidence for super-saturation in a quenched foil specimen. A drawback of the splat quenching technique is that it requires consolidation of quenched powders or foils. Thursfield and Stowell [23] consolidated the splat-quenched foils with hot extrusion and reported that the microstructure consisted of two zones with a size of approximately 100 μm: zone A consisted of Al grains, saturated with Fe and containing a very fine network sub-structure of metastable iron–aluminum intermetallic particles, while in zone B, particles of the equilibrium phase, $FeAl_3$, and the metastable phase, $FeAl_6$, were embedded in the matrix. Their mechanical characteristics are also listed in Table 1. As seen from Table 1, the present Al–Fe alloys exhibit a better strength and ductility balance as compared to the high-strength Al alloys reported previously. The superior mechanical properties may arise from the nano-scaled grain size and the absence of detectable levels of second-phase particles.

The variation of the yield stress at the quasi-static strain rate as a function of the concentration of alloying element in aluminum is shown in Fig. 13. Also plotted in this figure for comparison are the data for Al–Fe [34] and Al–Cr [37] fabricated by vapor quenching followed by rolling, splat-quenched Al–Fe alloy followed by extrusion [22], and extruded Al–Mg alloy [40]. As can be seen in this figure, the flow stress of binary Al alloys increases with increasing concentration of the alloying element. It should be noted that both the second-phase content and grain size are different for the different alloying additions shown in Fig. 13, owing to the differences in the processing methods employed. Consequently, the sole effect of solid-solution strengthening cannot be assessed from the comparison of the results plotted in this figure. The overall dependence of flow stress on the concentration of the alloying element varies with the type of element and processing; nevertheless, it is seen that the slope for Al–Fe and Al–Cr alloys is higher than that of Al–Mg.

King [41] defined the size effect on solid-solution strengthening by relating it to the atomic size factor, which is determined from the atomic volumes of aluminum and solute atoms. Noble et al. [42] showed the connection between solid-solution strengthening and atomic misfit factor in aluminum by using the atomic size factor. Alloying with Cr or Fe is more effective for strengthening than with Mg owing to the larger extent of lattice straining

Table 1
A survey of effects of processing and alloying on the quasi-static tensile response of high-strength Al alloys

Alloys (at.%)	Fabrication	Grain size (nm)	Dispersion size (nm)	Yield strength (MPa)	Tensile strength (MPa)	Elongation (%)	Ref.
5083 Al	Mechanical alloying	30		334	462	8.4	[7]
Al–5.9Ti–0.9Cu	Cryomilling	50 + 400[a]		600	725	3	[8]
Al–Cu–Mg–Ag–Mm	Spray deposition			480	530	–	[39]
Al–9.5Zn–3.0Mg–1.5Cu–4.0Mm–0.04Ag	Atomization	900		900	910	0.7	[35]
Al–Ni–Mm–Zr	NC powder consolidation	100	80	875	900	2.5	[9]
Al–Ni–Mm	Amorphous crystallization	70	70	825	850	1.2	[10]
Al–1.7Fe	VQ + rolling[b]		100–200	–	636	10	[33]
Al–2.1Fe	VQ + rolling		50–200	426	534	12.5	[34]
Al–3.7Fe	VQ + rolling		Layered	770	804	0.5	[34]
Al–3.6Fe	VQ + rolling		50–200	560	580	15	[34]
Al–3.9Fe	VQ + rolling		50–200	557	579	10	[34]
Al–4.0Fe	Splat quenching			503	570	5	[22]
Al–4Fe–0.8Ce	Atomization			465	590	7	[23]
Al–7.2Fe–1.2V	Melt spun		50–100	–	620	5	[24]
Al–5.3Cr	VQ + rolling			564	590	10.4	[37]
Al–0.4Cr–0.6Fe	VQ + rolling			655	679	10	[37]
Al–3.3Cr–0.5Fe	VQ + rolling			615	620	8	[37]
Al–4.2Cr–0.6Fe	VQ			559	563	4	[37]
Al–4.2Cr–0.6Fe	VQ + rolling			679	719	10	[37]
Al–4.5Cr–0.7Fe	VQ + rolling			818	831	6.7	[37]
Al–5.2Cr–0.8Fe	VQ			652	686	20	[36]
Al–5.2Cr–0.9Fe	VQ + rolling			575	712	5.5	[36]
Al–2.8Mm	VQ + rolling			–	455	4.2	[33]
Al–1.2Fe	VQ	95	–	687	688	11	This study
Al–1.5Fe	VQ	90	–	783	836	7	This study
Al–1.7Fe	VQ	85	–	842	897	6	This study

[a] Grain size quoted here is the average value of the reported grain size range.
[b] VQ refers to vapor-quenched material.

by Cr or Fe [36]. From the experimental results of Al–Fe in Fig. 13, it is seen that Fe is more effective for strengthening aluminum than such alloying elements as Cr or Mg, although the strength varies with the fabrication method and grain size. The Al–Fe alloys fabricated by splat-quench followed by extrusion were found to form the equilibrium phase of $FeAl_3$ and metastable iron–aluminum intermetallic particles [22].

Nasu et al. [38] examined the ^{57}Fe Mössbauer spectra in splat quenched Al–Fe alloys, and showed that the fraction of isolated iron atom was ~89% and that the remaining Fe atoms formed atomic clusters in the Al–1 at.% Fe alloy. The present Al–Fe alloys consist of 1.15–1.71 at.% of iron in the super-saturated solid solution without second-phase particles as shown in Fig. 8. Thus, these alloys possibly contain atomic clusters of Fe.

The observed flow stress levels in the present Al–Fe alloys far exceed those predicted solely on the basis of grain size strengthening. For example, if Hall–Petch strengthening were to be responsible

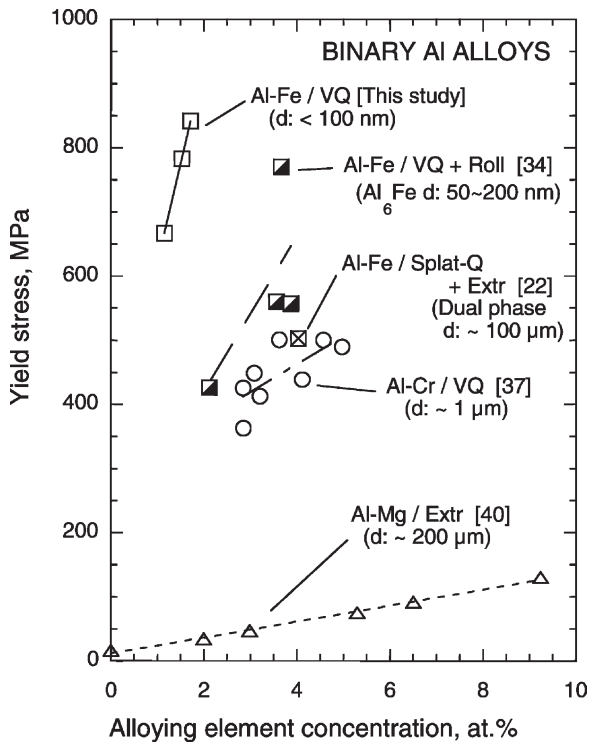

Fig. 13. Variation of yield stress as a function of concentration of the alloying element in the aluminum matrix. Including are the data of Al–Fe [34] and Al–Cr [37] fabricated by vapor quenching, splat quenching of Al–Fe alloy followed by extrusion [22], and extruded Al–Mg alloy [40].

for the flow resistance down to a sub-grain size of 85 nm, the expected contribution to the overall strength from grain refinement in pure aluminum would be approximately 250 MPa [10]. This value is much smaller than the value of 783 MPa measured for the Al–1.5Fe alloy.

The effect of strain rate on the hardening behavior of the present Al–Fe alloys is different from that reported for conventional Al alloys. It has been found that the strain-hardening rate in Al alloys remains essentially unchanged over a wide range of strain rate at ambient temperature [43]. The present results, however, show trends similar to the strain-hardening behavior at quasi-static strain rate reported for an ECAP-processed Al–Mg alloy. For the sub-microcrystalline Al–Mg alloy, the shape of the stress–strain curve is almost unchanged over a wide range of strain rate: the alloy also exhibited limited strain hardening but large elongation prior to failure at both quasi-static and dynamic strain rates [44]. These experimental results support the notion that the ratio of newly generated to annihilated dislocations remains unchanged by the deformation rate. On the other hand, the hardening rate of the present Al–Fe alloys varies with strain rate. The hardening rate at the dynamic strain rate maintains a positive value, while that at the quasi-static strain rate shows a negative value at an early stage of deformation (at a plastic strain of ~0.01). The mechanisms underlying such effects are not fully evident from the present observations.

The fracture surface features seen for the present Al–Fe alloys are similar to the failure processes observed in nanocrystalline pure Ni at strain rates of 10^{-5} and 1 s^{-1} [31]. These fracture surface features are also similar to those observed in pure NC Ni following tension and compression deformation at quasi-static strain rates, and during in situ tensile fracture induced inside a transmission electron microscope [45]. This latter study also revealed that dislocation emission at grain boundaries in conjunction with intragranular slip and unaccommodated grain boundary sliding facilitates the formation of voids at grain boundaries and triple junctions, which act as nucleation sites for the dimples.

5. Conclusions

Solid-solution Al–Fe binary alloys, with iron content from 1.15 to 1.71 at.%, were processed by electron-beam deposition, to produce a sub-grain structure with a grain size typically smaller than 100 nm within a polycrystalline solid-solution aluminum matrix comprising micron-sized high-angle grain boundaries. The strength of the as-deposited alloy was found to increase with increasing Fe content. The as-deposited Al–1.71 at.% Fe alloy showed an abnormally high tensile strength of approximately 950 MPa and a ductility of approximately 6% in tension at a dynamic strain rate of 1.1×10^3 s^{-1}. The yield stress was found to be essentially independent of strain rate, while the tensile strength showed strain-rate sensitivity. Detailed inspection of microstructure at atomic resolution revealed that nano-scale discontinuities within the aluminum lattice, possibly arising from the presence of solute

atom clusters or defects, were formed in the interior of the sub-grains. These structural features in conjunction with the nanocrystalline sub-grains and the ostensible absence of any second-phase particles appear to impart significant strength to the alloy, while the presence of the high-angle boundaries seems to promote a reasonable level of ductility in the alloy. The fracture surfaces of the alloys exhibited a ductile failure mode wherein dimples, spanning five to 10 grain diameters, were formed under both quasi-static and dynamic tension.

Acknowledgements

This work was supported by the Defense University Research Initiative on Nano Technology (DURINT) on "Damage- and Failure-Resistant Nanostructured and Interfacial Materials" which is funded at the Massachusetts Institute of Technology (MIT) by the Office of Naval Research under grant N00014-01-1-0808. Special thanks are due to Dr J.-J. Kim of MIT for his help in obtaining Fig. 7, to Dr Koichi Ishikawa and Mr Hiroyuki Watanabe of Osaka Municipal Technical Research Institute, Japan, for their help with some of the tensile tests, to Prof. K.S. Kumar of Brown University for his useful comments on the manuscript and to Dr A. Tony Garrett-Reed of MIT for his helpful suggestions.

References

[1] Weertman JR. Mater Sci Eng A 1993;166:161.
[2] Sanders PG, Eastman JA, Weertman JR. Acta Mater 1997;45:4019.
[3] Sun XK, Cong HT, Sun M, Yang MC. Nanostruct Mater 1999;11:917.
[4] Carsley JE, Fisher A, Milligan WW, Aifantis EC. Metall Mater Trans 1998;29A:2261.
[5] Jia D, Ramesh KT, Ma E. Scr Mater 2000;42:73.
[6] Hwang S, Nishimura C, McCormick PG. Scr Mater 2001;44:1507.
[7] Tellkamp VL, Melmed A, Lavernia EJ. Metall Mater Trans 2001;32A:2335.
[8] Hayes RW, Rodriguez R, Lavernia EJ. Acta Mater 2001;49:4055.
[9] Nagahama H, Ohtera K, Higashi K, Inoue A, Masumoto T. Philos Mag Lett 1993;67:225.
[10] Mukai T, Higashi K. Scr Mater 2001;44:1493.
[11] Popov AA, Pyshmintsev IY, Demakov SL, Illarionov AG, Lowe TC, Sergeyeva AV et al. Scr Mater 1997;37:1089.
[12] Noskova NI, Volkova EG. Phys Met Metallogr 2001;91:629.
[13] Xiao C, Mirshams RA, Whang SH, Yin WM. Mater Sci Eng A 2001;301:35.
[14] Yin WM, Whang SH, Mirshams R, Xiao CH. Mater Sci Eng A 2001;301:18.
[15] Lu L, Li SX, Lu K. Scr Mater 2001;45:1163.
[16] Sasaki H, Kita K, Nagahora J, Inoue A. Mater Trans 2001;42:1561.
[17] Gray III GT, Lowe TC, Cady CM, Valiev RZ, Aleksandrov IV. Nanostruct Mater 1997;9:477.
[18] Jia D, Ramesh KT, Ma E, Lu L, Lu K. Scr Mater 2001;45:613.
[19] McFadden SX, Mishra RS, Valiev RZ, Zhilaev AP, Mukherjee AK. Nature 1999;398:684.
[20] Jones H. Mater Sci Eng 1969–1970;5:1.
[21] Furrer P, Warlimont H. Z Metallkd 1973;64:236.
[22] Jacobs MH, Doggett AG, Stowell MJ. J Mater Sci 1974;9:1631.
[23] Thursfield G, Stowell MJ. J Mater Sci 1974;9:1644.
[24] Skinner DJ, Okazaki K. Scr Metall 1984;18:905.
[25] Nicholas T, Bless SJ. High strain-rate tension testing. In: Mechanical testing. ASM handbook, vol. 8. American Society of Metallurgists; 1985. p. 208.
[26] Senseny PE, Duffy J, Hawley RH. J Appl Mech 1978;45:60.
[27] Lindholm US, Bessey RL, Smith GV. J Mater 1971;6:119.
[28] Frantz RA, Duffy J. J Appl Mech 1972;39:939.
[29] Mukai T, Kawazoe M, Higashi K. Nanostruct Mater 1998;10:755.
[30] Mukai T, Ishikawa K, Higashi K. Metall Mater Trans 1995;26A:2521.
[31] Kwon YN, Suresh S. Unpublished research, Massachusetts Institute of Technology, Cambridge, MA.
[32] Lu L, Sui ML, Lu K. Science 2000;287:1463.
[33] Partridge PG. J Mater Sci 1986;21:3211.
[34] Bickerdike RL, Clark D, Easterbrook JN, Hughes G, Mair WN, Partridge PG et al. Int J Rapid Solidif 1985–1986;1:305.
[35] Adachi H. Scr Mater 2001;44:1489.
[36] Bickerdike RL, Clark D, Easterbrook JN, Hughes G, Mair WN, Partridge PG et al. Int J Rapid Solidif 1986;2:1.
[37] Partridge PG, McConnell MC. Acta Metall 1987;35:1981.
[38] Nasu S, Gonser U, Shingu PH, Murakami Y. J Phys F Met Phys 1974;4:L24.
[39] Del Castillo L, Lanernia EJ. Metall Mater Trans 2000;31A:2287.
[40] Mukai T, Higashi K, Tanimura S. Mater Sci Eng A 1994;176:181.
[41] King HW. J Mater Sci 1966;1:79.
[42] Noble B, Harris SJ, Dinsdale K. J Mater Sci 1982;17:461.
[43] Johnson GR, Hoegfeldt JM, Lindholm US, Nagy A. J Eng Mater Technol Trans ASME 1983;105:48.
[44] Mukai T, Kawazoe M, Higashi K. Mater Sci Eng A 1998;247:270.
[45] Kumar KS, Suresh S, Chisholm MF, Horton JA, Wang P. Acta Mater 2003;51:387.